TÜBİTAK

Turkish Journal of Earth Sciences

http://journals.tubitak.gov.tr/earth/

Research Article

Turkish J Earth Sci
(2014) 23: 277-292

doi:10.3906/yer-1306-12

Appraisal of active tectonics using DEM-based hypsometric integral and trend surface analysis in Emilia-Romagna Apennines, northern Italy

Saima SIDDIQUI[1,2,*], Mauro SOLDATI[1]

[1]Department of Chemical and Geological Sciences, University of Modena and Reggio Emilia, Modena, Italy
[2]Centre for Integrated Mountain Research, University of the Punjab, Lahore, Pakistan

Received: 22.06.2013 • **Accepted:** 17.01.2014 • **Published Online:** 21.03.2014 • **Printed:** 18.04.2014

Abstract: The hypsometric integral (HI) has generally been used to explain the stages of landscape evolution and erosional processes. It is an important tool to investigate tectonics and lithologic and climatic effects on topographic change. We analyzed the significance of the HI to investigate active tectonics in the Emilia-Romagna Apennines of northern Italy. We used a digital elevation model of 5-m spatial resolution to calculate grid-based HI values. The HI distribution does not show clear spatial patterns of high and low HI values. However, when statistical methods of local indices of spatial autocorrelation were applied, it was possible to identify clear clusters of high and low HI values. Trend surface analysis (TSA) was carried out to distinguish areas with anomalously high and low elevations, and to observe their spatial correlation with the HI and regional geological structures. The results indicate that the high HI values and TSA anomalies are positively correlated with the areas of high tectonic activity and along the regional tectonic structures.

Key words: Digital elevation model, hypsometric integral, local indices of spatial autocorrelation, trend surface, active tectonics, Emilia-Romagna Apennines, northern Italy

1. Introduction

Hypsometry pertains to the relative proportion of an area at different elevations of the earth's surface (Strahler, 1952). Hypsometry can be evaluated through the hypsometric curve (HC) and hypsometric integral (HI). HCs and HIs can be explained in terms of the degree of landscape (basin) dissection and relative landform age. Hypsometric analysis is typically used to evaluate the rate of catchment erosion, geomorphic stages of landscape evolution, and dissection processes and, more generally, to identify and explain the denudation and tectonic processes over a region. Weissel et al. (1994) suggested that hypsometry may reveal the interaction between erosion and tectonics and could provide a considerable geomorphic index that constrains the relative importance of these processes. Hypsometric integral analysis has been used in several studies such as geology, geomorphology, hydrology, glaciology, tectonics, and climatology (Lifton and Chase, 1992; Ohmori, 1993; Masek et al., 1994; Chen et al., 2003; Walcott and Summerfield, 2008; Pérez-Peña et al., 2009a, 2009b; Rutledge and Christensen, 2010).

Trend surface analysis (TSA) is a procedure to derive a continuous smooth surface from irregular data to isolate regional trends from local variations (Grohmann, 2005; Garrote et al., 2008). TSA is appropriate for regional data such as delineating an ancient, dissected erosional surface or the paleoflow direction of a good-sized watershed. The ultimate objective of this study is to demarcate zones of relative tectonic activity by examining regional topography. The geographic information system (GIS) approach was used to calculate the HI and associated parameters. The spatial autocorrelation analysis of grid-based HIs and TSA is a powerful tool to discriminate areas affected by recent tectonic activity or differential erosion.

2. Study area

The study area is located in the northern Apennines (Figure 1a), mainly in the provinces of Reggio Emilia, Modena, and Bologna, extending from the Tuscan-Emilia watershed in the southwest to the Pede-Apennine margin in the northeast. Mt. Cimone (2165 m) is the highest peak of the entire northern Apennines and is located in this region. The Secchia, Panaro, and Reno are the main rivers flowing transverse to the mountain chain (Figure 1b).

3. Geological setting

The northern Apennines is a complex fold and thrust postcollisional NW-SE–oriented mountain chain, which

* Correspondence: saimagct@gmail.com

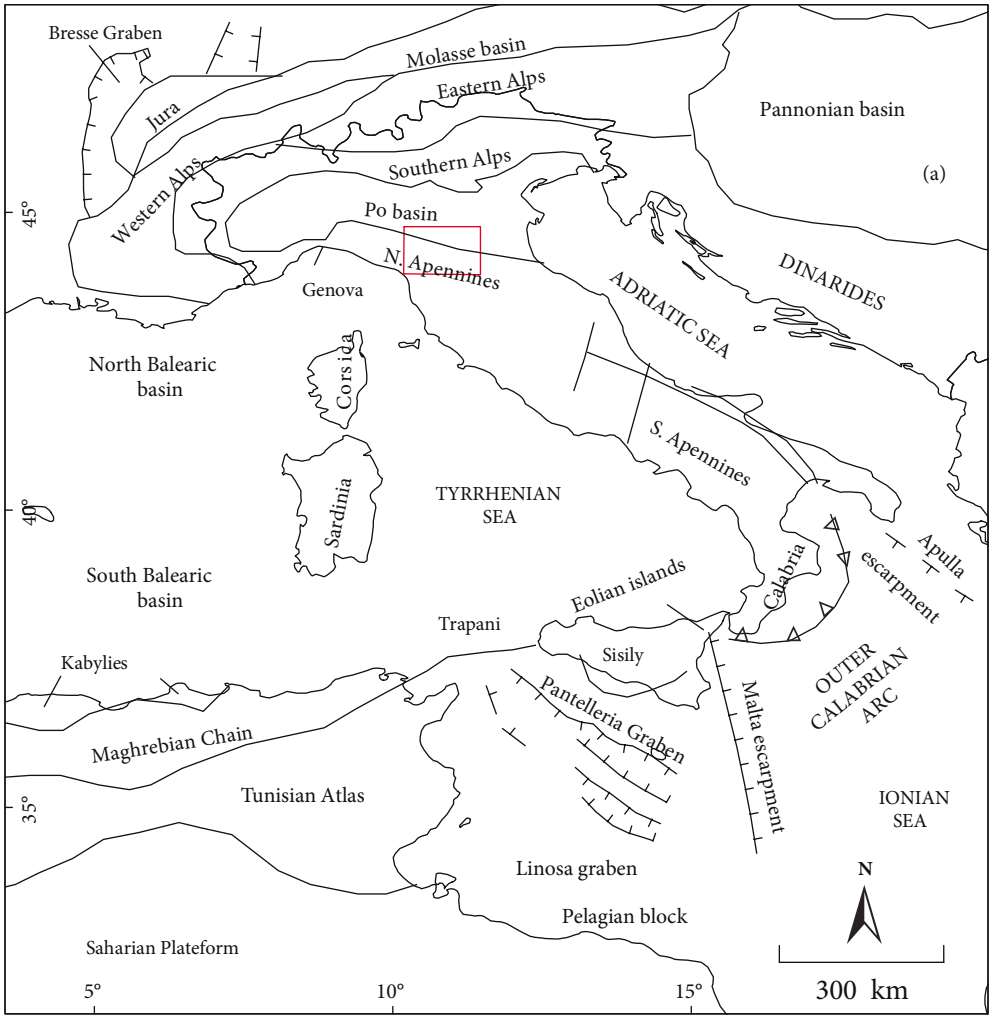

Figure 1. a) Outline map of Italy and surrounding region showing the major tectonic elements (modified from Vai and Martini, 2001), with red rectangle showing the general location of the study area; b) 5-m spatial resolution DEM for the studied basins of the Secchia, Panaro, and Reno rivers. The black boundary shows the study area and main rivers are shown with blue lines.

formed during the Tertiary due to ongoing convergence between the European and Adria plates (Elter, 1960; Boccaletti et al., 1971; Boccaletti and Guazzone, 1972; Reutter and Groscurth, 1978; Boccaletti et al., 1981; Bettelli and De Nardo, 2001; Cerrina Feroni et al., 2002). With reference to the Po Plain, all of the northern Apennines belt is actively being uplifted at rates ranging from 0.1 to 2 mm/year (Spagnolo and Pazzaglia, 2005). The northern Apennines mountain front and its adjacent foothills are riddled with geomorphic and geologic evidence of recent tectonics such as active folds and faults (Picotti and Pazzaglia, 2008). However, information on the recent and active structures remains limited to scattered areas (Piccinini et al., 2006; Picotti and Pazzaglia, 2008; Picotti et al., 2009; Wilson et al., 2009). The study area is characterized by complex structures showing the presence of different fault systems of tectonic origin (Bettelli et al., 2002a, 2002b; Panini et al., 2002a, 2002b; Plesi et al., 2002a, 2002b; Severi et al., 2002a, 2002b; Balocchi, 2003; Boccaletti et al., 2004b). These tectonic structures can be divided into 2 groups based on their direction with respect to the Apennine watershed: the anti-Apenninic (NE-SW) transverse fault systems and NW-SE–oriented fault systems parallel to the main Apenninic divide (Figure 2).

The Emilia-Romagna portion of the northern Apennines represents the part of the orogen that is still shortening, with a deformation front buried beneath Quaternary sediments of the Po foreland. Rocks in the uplifted and exposed portion of the orogenic wedge are Mesozoic carbonates and Cenozoic, mostly turbiditic sandstone, siltstone, mudstone, and marls deposited in shelf slope-trench basins in front of and atop a thrust-

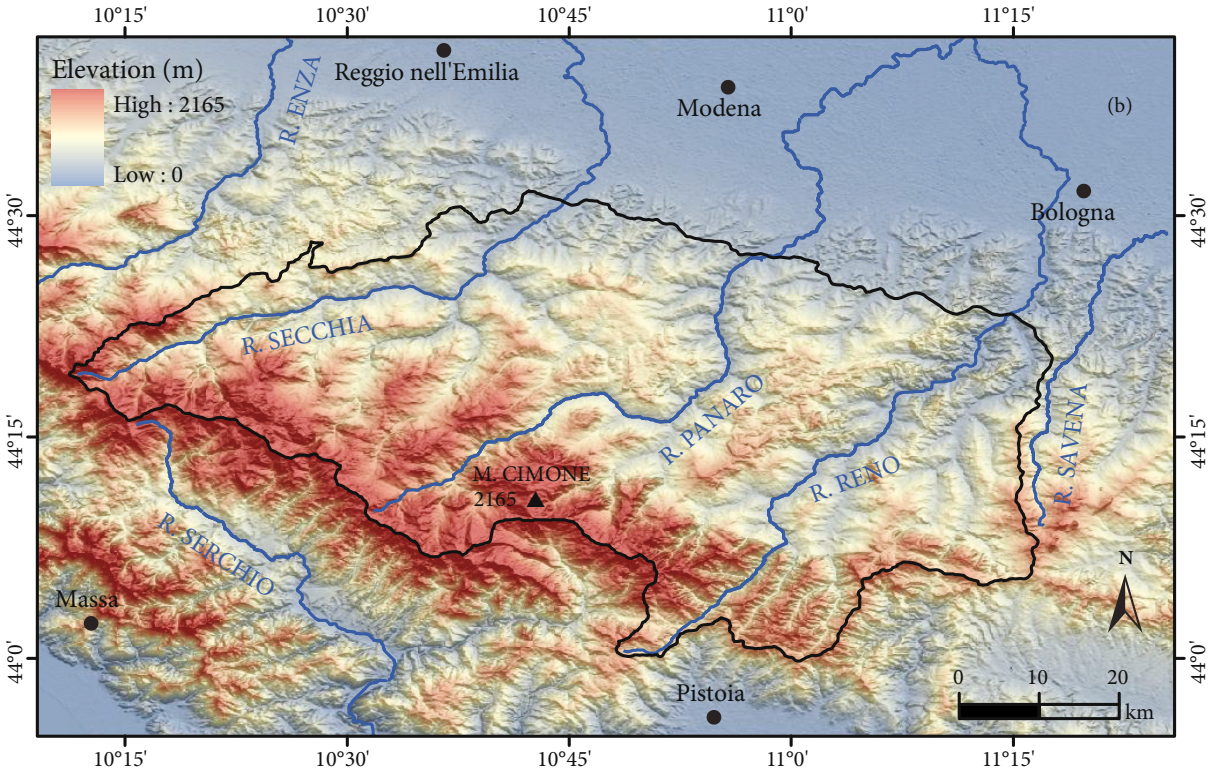

Figure 1. (continued).

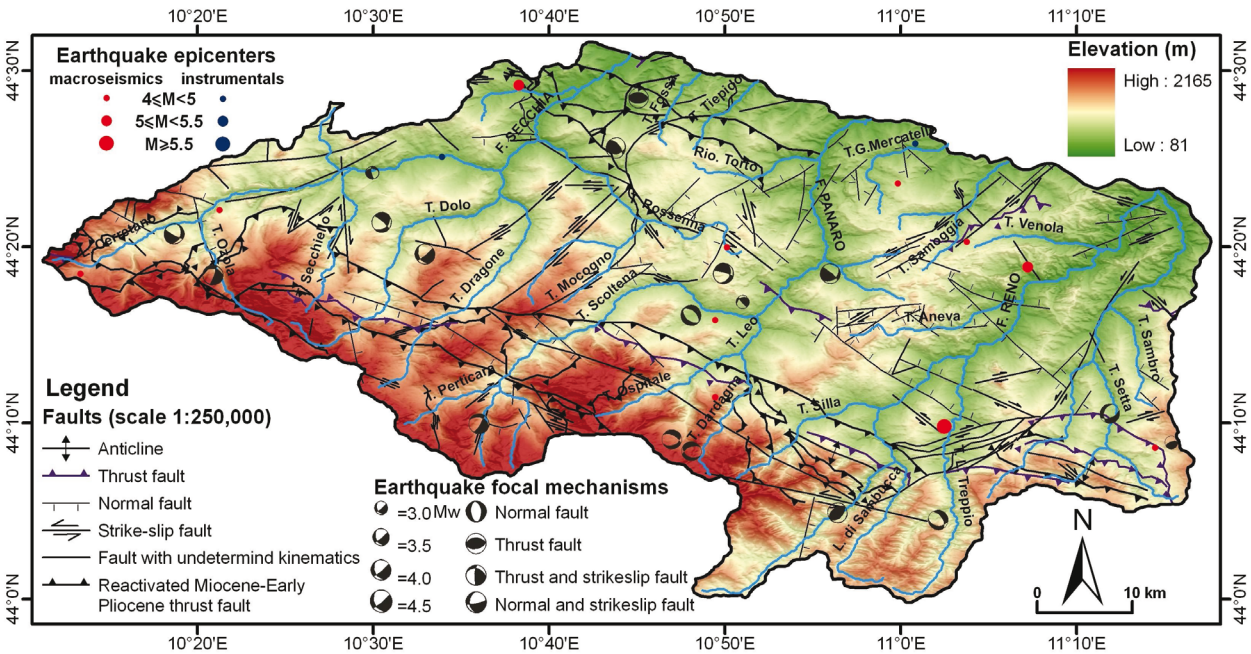

Figure 2. Digital elevation model showing distribution of focal mechanism solutions, earthquake epicenters, and major tectonic structures of the study area (modified from Boccaletti et al., 2004b).

imbricated Mesozoic platform carbonate basement. These siliciclastic rocks have now been frontally accreted and incorporated into the wedge. In the Emilia part of the range, the Cenozoic turbidites remain buried beneath a largely intact structural lid called the Ligurian nappe, which represents a large thrust panel composed of Mesozoic ophiolite basement, Mesozoic marine siliciclastics and carbonates, and epi-Ligurian (wedge-top), shelf-slope

siliciclastic basins. Rock resistance is generally lower in the Emilia Apennines in comparison to the Romagna Apennines, except for some of the high-elevation portion near the drainage divide. Here, siliciclastic turbidites, the Macigno and Cervarola formations, similar in grain size and bedding characteristics to the younger Marnosa Arenacea, outcrop as resistant cliff-formers (Cerrina Feroni et al., 2001; Spagnolo and Pazzaglia, 2005). The study area is also characterized by numerous landslides (Bertolini and Pellegrini, 2001; Trigila, 2007) of all types (according to the classification of Cruden and Varnes, 1996) consistent with steep slopes, weak rock type, and the existing underlying structural settings.

4. Methodology

4.1. Hypsometric curve and hypsometric integral

The study of HCs and HIs has been performed to differentiate between erosional landforms at different stages during their evolution (Strahler, 1952b; Schumm, 1956; Ohmori, 1993; Willgoose and Hancock, 1998; Keller and Pinter, 2002; Chen et al., 2003; Omvir, 2009; Pérez-Peña et al., 2009a, 2009b). The HC (Langbein, 1947; Strahler, 1952) depicts the distribution of a basin area with altitude, typically as a proportion of an area above a unit of elevation (Figure 3a). The shape of the HC and HI values provides vital information about erosional stages of the relief and tectonic, climatic, and lithological factors controlling landforms' development (Moglen and Bras, 1995; Willgoose and Hancock, 1998; Huang and Niemann, 2006). Convex-up curves are typical for the "disequilibrium" stage (or youthful stage), typified by rugged terrain and deep incision; smooth, S-shaped curves crossing almost the center of the diagram typify "equilibrium" landscapes (or mature stage); and concave-up curves typify the "peneplain" stage (or old stage), characterized by land near base level with extremely subdued relief (Strahler, 1952b; Schumm, 1956; Chen et al., 2003; Pérez-Peña et al., 2009a; Figure 3a). These stages of landscape evolution are based on the assumption that wherever active deformation and uplift rates dominate over erosion, the elevation and topography increase.

The HI is a dimensionless number that allows different watersheds to be compared regardless of scale [Eq. (1)]. The HI value could reflect both tectonic activity and lithological control (Lifton and Chase, 1992; Hurtrez and Lucazeau, 1999; Chen et al., 2003), and it might be a capable tool that can differentiate these 2 aspects. Lifton and Chase (1992) tested the influence of variable uplift rates on hypsometry from a numerical model of landscape development, showing that the hypsometric integral was positively correlated to the uplift rate. The HI value is the area below the HC, which relates the percentage of total available relief to the cumulative percentage of area (Figure 3b) and, therefore, is similar to the shape of the HC (Pike and Wilson, 1971; Mayer, 1990; Keller and Pinter, 2002; Pérez-Peña et al., 2009b). The value of the HI varies from 0 to 1 (Harrison et al., 1983); high HI values (≥0.55) correspond to less eroded "young" landscapes where tectonic processes are dominant as compared to erosion, low values (≤0.35) are related to old, highly eroded landscapes, and intermediate HI values (~0.5) are associated with a balance (dynamic equilibrium) between erosion and tectonic processes (Strahler, 1952b; Mayer, 1990; Keller and Pinter, 2002).

HI analysis using digital elevation model (DEMs) is handy because it is a dimensionless parameter and allows various watersheds to be analyzed and compared irrespective of basin area or shape (Strahler, 1952b; Keller and Pinter, 2002; Walcott and Summerfield, 2008). A GIS provides significant tools for the computation of spatial parameters (e.g., area, altitude, perimeter, length, width) and facilitates extraction of valuable morphometric information, especially through the use of DEMs.

4.2. Computer estimation of hypsometric integral

Following the methodology of Pérez-Peña et al. (2009b), we computed HI values for the Secchia, Panaro, and Reno mountain river basins using a DEM of 5-m spatial resolution. The DEM was pit/depression-filled using ArcGIS 9.3 software. The HI values were computed using analysis grid size of 1 km, since this grid scale can obtain

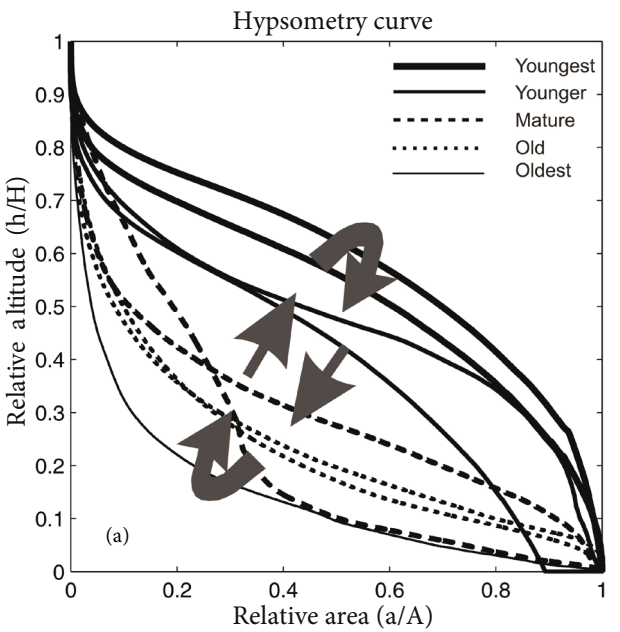

Figure 3. a) Hypsometric curves showing the geomorphic cycle of landscape development, where changes in the shape of the curve indicate different stages of landscape evolution (modified from Ohmori, 1993); b) diagram shows procedure for calculating hypsometric curves using percentage height (h/H) and percentage area relationship (a/A) (modified from Luo, 1998).

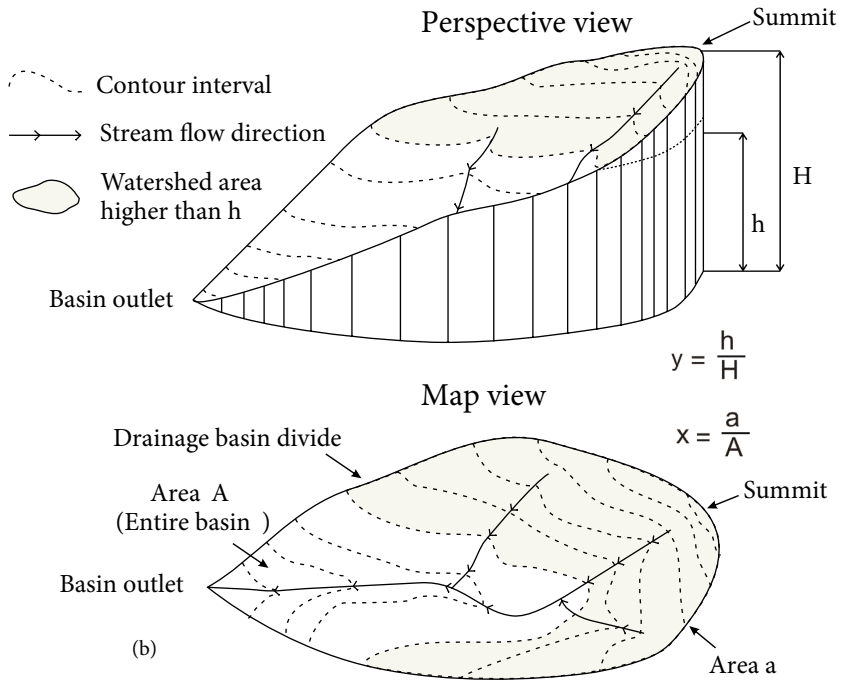

Figure 3. (continued).

significant topographic information of the area under investigation (Pike and Wilson, 1971; Keller and Pinter, 2002; Luo, 2002; Chen et al., 2003; Pérez-Peña et al., 2009b; Blanchard et al., 2010). In order to obtain HI values, we prepared regular 1-km-sized grids using the ArcGIS 9.3 spatial analysis tool (Figures 4a and 4b). Using a zonal statistics tool, we extracted the maximum, minimum, and mean elevation from DEMs for each grid cell. Pike and Wilson (1971) mathematically proved that the elevation-relief ratio (mean elevation – minimum elevation/ maximum elevation – minimum elevation) can be a valid proxy to the HI and has the benefit of being easier to obtain numerically. Therefore, in this study, we computed HI values using the following equation:

$$HI = \frac{H_{mean} - H_{\min}}{H_{\max} - H_{\min}} \quad (1)$$

In this study, we do not analyze catchments of different order, and so instead of representing a measure of landscape dissection, the HI values indicate how quickly elevation varies within each square (van der Beek and Braun, 1998). Using this methodology, we can obtain HI values independent of catchment area and geometry. The HI values can vary from high to low across adjacent cells due to the complexity of deformation processes and variable erosion rates (Figures 5a and 5b). The variations in HI values did not show significant patterns; for this reason, we used the local indices of spatial autocorrelation (LISA) technique (Moran, 1950; Anselin, 1995; Getis and Ord, 1996; Ratcliffe and McCullagh, 1998) to distinguish clusters of high and low HI values. In the case of tectonic activity, the clusters of high HI values should show a general spatial pattern in correspondence to neotectonically active areas (Pérez-Peña et al., 2009b).

4.3. Spatial autocorrelation using Moran's I and Getis-Ord Gi*-statistics

Spatial autocorrelation analysis is helpful in investigating spatial association in georeferenced datasets (Moran, 1950; Cliff and Ord, 1981; Haining, 1990; Anselin, 1995; Chou, 1997; Ratcliffe and McCullagh, 1998; Diniz-Filho et al., 2003; Yu and Wu, 2004; Pérez-Peña et al., 2009b). Spatial autocorrelation measures the degree of sameness of spatially distributed values of a single variable (e.g., HI values) within their neighborhood. In the last decades, these statistics have been significantly used for spatial autocorrelation analysis in many different disciplines, e.g., remote sensing investigations (Wulder and Boots, 1998), criminology (Ratcliffe and McCullagh, 1998), sociology (Unwin, 1996; Amrhein and Reynolds, 1997), ecology (Diniz-Filho et al., 2003), and tectonic geomorphology (Pérez-Peña et al., 2009b). The global Moran index (Moran, 1950) can be used to measure the spatial autocorrelation of any variable (HI values in this study). This statistic shows the extent to which points that are "close together" in space have similar values on average. It estimates whether the set of attributes are random, dispersed, or clustered (Figure 6). Moran's I can be computed using following formula:

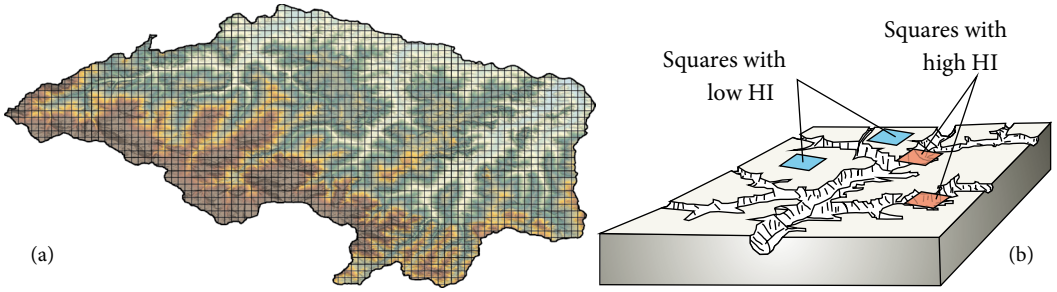

Figure 4. Schematic diagram showing HI value computations from DEM using regular-sized analysis grid: a) division of DEM into regular squares; b) the HI values show high variation due to the location of squares (modified from Pérez-Peña et al., 2009b).

$$I = \frac{N\sum_i\sum_j w_{ij}(x_i - \bar{x})(x_j - \bar{x})}{\left(\sum_i\sum_j w_{ij}\right)\sum_i (x_i - \bar{x})^2} \quad (2)$$

where N = the number of cases, $\bar{x}$ = the mean of the attribute of interest, x_i = the measured attribute of interest at location i, x_j = the measured attribute of interest at location j, and w_{ij} = a weight indexing the location of i relative to j.

The expected value of Moran's I or *E(I)* is calculated using –1/(N – 1), by assuming that the values are randomly distributed. This is generally very close to 0, and so for all practical purposes, a value of 0 is used to indicate a random distribution. Results for Moran's I (*MI*) range from –1 to 1. If more pairs of neighboring values have similar values, then the sum of the cross-products will be positive and *MI* will be greater than 0, indicating positive spatial autocorrelation in which similar values, either high or low, are spatially clustered. Similarly, if *MI* is less than 0 and close to –1, it indicates negative spatial autocorrelation, in which neighboring values are dissimilar and completely dispersed (Figure 6).

In ArcGIS, the *Z*-score and P-value are calculated to indicate the confidence level that any pattern of positive or negative association is not just due to chance (Anselin, 1995). For this purpose, the GIS uses the following formula:

$$Z - score = \frac{I - E(I)}{S_{E(I)}} \quad (3)$$

where *E(I)* is equal to –1/(N – 1) under the assumption of no autocorrelation, and $S_{E(I)}$ is the standard deviation based on the number of data points, the number of

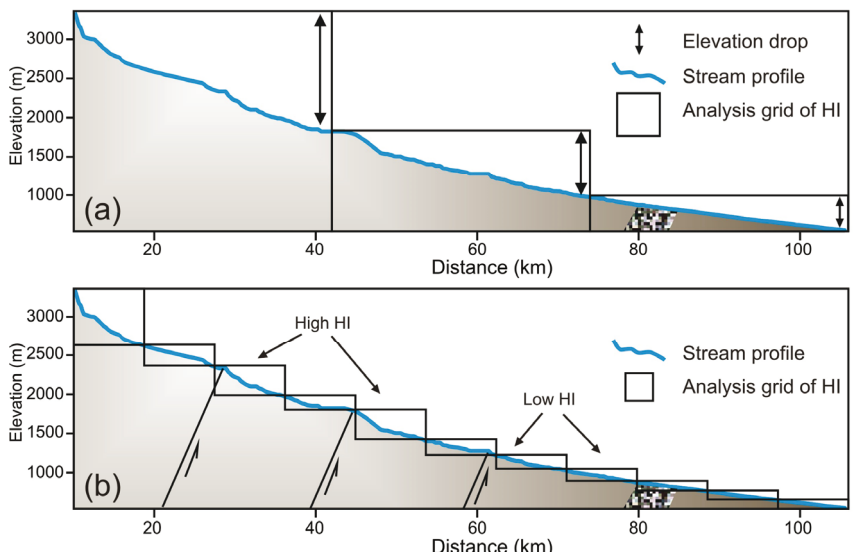

Figure 5. Schematic illustration showing spatial dependency of hypsometric integral: a) change in HI values due to drop in elevation from upstream reach to downstream reach; b) small-sized square areas or catchment units can significantly determine local variations due to tectonic activity or lithological change (modified from Chen et al., 2003).

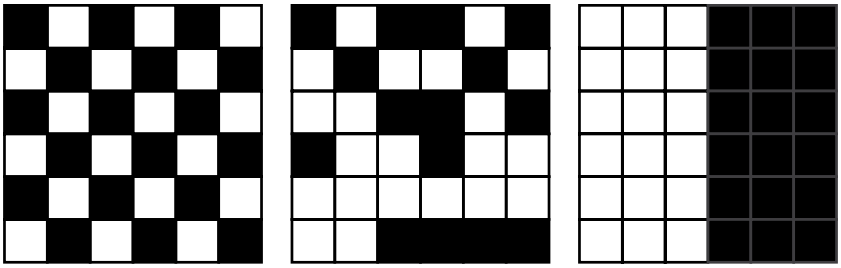

Figure 6. Diagrams showing types of data distribution and Moran's I statistics showing spatial association or spatial autocorrelation.

neighboring features, and the sum of the weight values. A positive Z-score indicates clustering, while a negative Z-score indicates dispersion. Moran's I only indicates whether similar values are clustered or dispersed; we could not tell from this analysis whether the clusters of data were composed of high values or low values.

In order to determine the concentration of high or low values around individual locations, we measured LISA statistics (Anselin, 1995; Getis and Ord, 1996). The General Gi*-statistic (Getis and Ord, 1996) indicates whether hot spots (clusters of high values) or cold spots (clusters of low values) exist within a specified distance in the entire study area. The Gi*-statistic is calculated using a neighborhood distance that we specify. If the "neighboring" feature is within the specified distance of the target feature, then that pair will be assigned a weight of 1; otherwise, the pair will be assigned a weight of 0. The high values of the Gi*-statistic corresponds to hot spots indicating high attribute values placed together in a location, while a low value corresponds to cold spots indicating low values that are placed together. The Gi*-statistic is calculated by summing the values of the neighbors and dividing them by the sum of all values in the study area:

$$G_i^* = \frac{\sum_j w_{ij}(d)x_j}{\sum_j x_j} \quad (4)$$

where x_j = the measured attribute of interest at location j, and w_{ij} = a weight indexing the location of i relative to j (this is 1 if locations i and j are within the specified distance and 0 if no distance is specified).

4.4. Trend polynomial surface analysis

TSA uses a polynomial regression to fit a least-squares surface to the input points. It involves the fitting of a surface (a polynomial model) through a set of points in X,Y,Z coordinate space. The fitted surface likely will not pass exactly through each point, and so least-squares regression is used to minimize the distance between measured Z-values and the fitted surface directly above or below. Differences are expressed as root mean square (RMS). The smaller the r-squared value, the closer the fit between points and surface (Grohmann, 2005). Polynomial order controls the complexity of the trend surface; high orders are more "flexible". Trend surfaces smooth local anomalies. A 1st-order polynomial surface is a tilted plane while a 12th-order polynomial is a highly complex surface.

5. Results

5.1. HI and spatial dependency analysis

The analysis reveals that HI values are normally distributed over the entire study area, showing a mean average value of ~0.5. (Figure 7). However, this spatial distribution of HI values does not show a clear pattern of high or low values due to high variation in local topographic relief. According to Chen et al. (2003), the HI values could be spatially dependent due to the relative position of grid cells on high or low relief in a region. In order to examine whether the variation in HI values are space- and scale-dependent, we compared 2 basin parameters i.e. the relief amplitude (RA) obtained by calculating the difference between maximum and minimum elevation, and the mean altitude (MA) with the respective HI value inside each square. The grid cells in the upper watershed areas represent high RA and MA values because of the steep gradients and high landscape dissection (Chen et al., 2003). The spatial dependency analysis of HI values indicates that the high to low HI values are fairly scattered around the HI mean value on HI vs. relief amplitude and HI vs. mean altitude plots (Figure 8). There is no correlation between the distribution of variable HI values and high or low RA and MA values. Nevertheless, when HI values were averaged and pinned on fixed intervals (50 m on relief amplitude and 150 m on mean altitude plot) along a horizontal axis, they followed an almost linear pattern, showing that HI values are not dependent on these factors (e.g., Walcott and Summerfield, 2008; Pérez-Peña et al., 2009b). Our results conform to the findings of previous work by Pérez-Peña et al. (2009b). We conclude that there is no correlation between HI values and spatial location of grid cells, which confirms that calculation of HI is not spatially dependent.

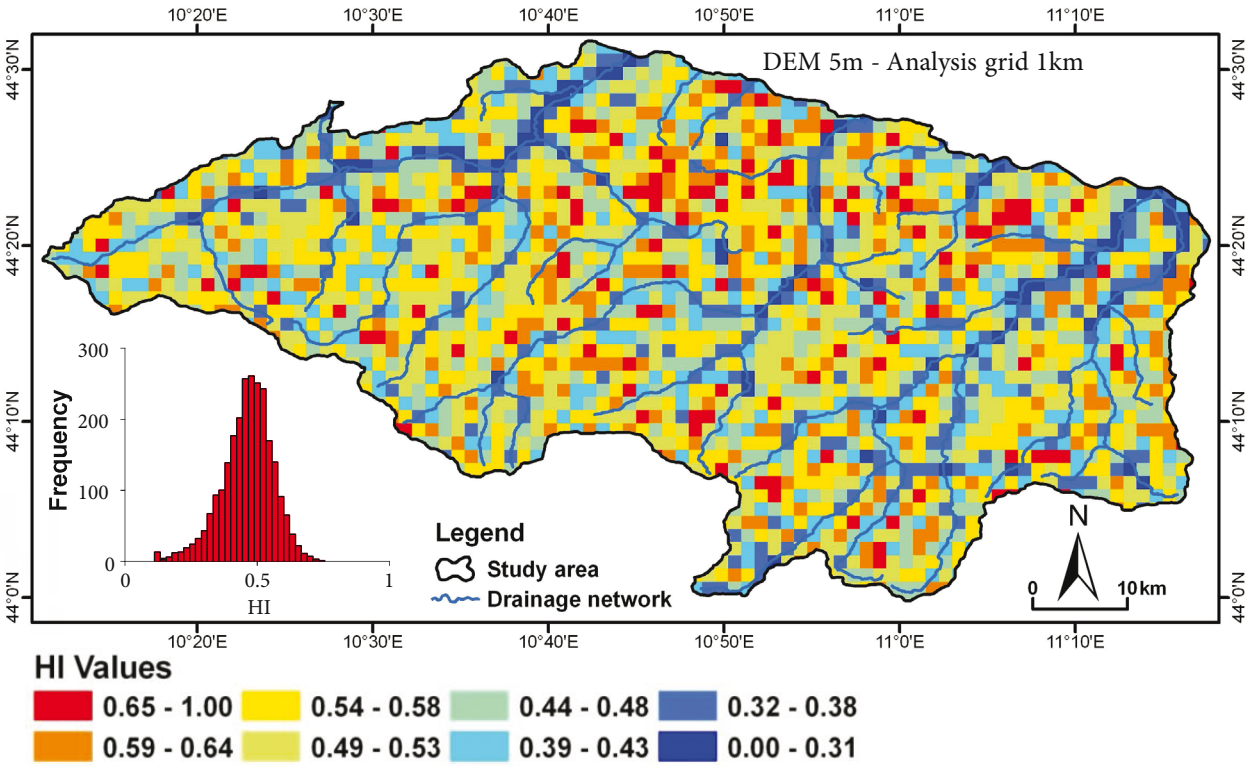

Figure 7. Spatial distribution of HI values extracted from DEM of 5-m spatial resolution using 1-km regular-sized analysis grid.

5.2. Lithological effects on HI values

To analyze the lithological influence on the distribution of HI values, we used a regional lithotechnical map (classified on the basis of similar rock properties and hardness levels from a 1:10,000 scale geological map). Because of the large study area and variable lithology, we did not carry out a thorough analysis of rock erodibility, but we correlated HI values (computed for the 1-km^2 grid using 5-m DEM) with the lithotechnical units (Table 1) of the study area. We obtained percentage lithology information for each 1-km^2 cell, and only those cells were considered for the comparison between HI values and lithological units where the main lithology covered more than 85% of the cell area (Figure 9a). For each lithological unit, we then computed the mean HI value and standard deviation of HI values from the mean value (Figure 9b). For each lithological

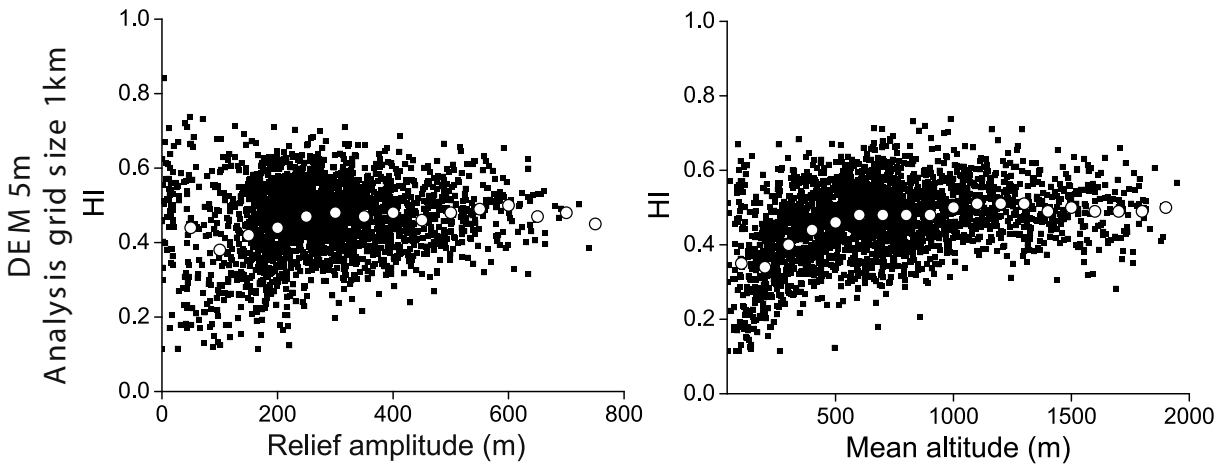

Figure 8. Hypsometric integral (HI) versus relief amplitude (RA) and mean altitude (MA); the distribution of HI values is not spatially dependent on RA and MA.

Table 1. Description of lithological units and rock strength levels.

Lithological unit	Description		
Gc	Gypsums in chaotic deposits	Low	
Dsc	Tectonized clays and argillites		
Dol	Olistostromic clays		
Dm	Marls		Rock strength level
Da	Consolidated clays		
Cs	Weakly cemented sands		
Cc	Clast-supported conglomerates		
Bp	Massive/pelitic alternations with L/p < 0.3		
Blp	Massive/pelitic alternations with 0.3 < L/p < 3		
Bl	Massive/pelitic alternations with L/p > 3		
As	Stratified massive rocks	High	

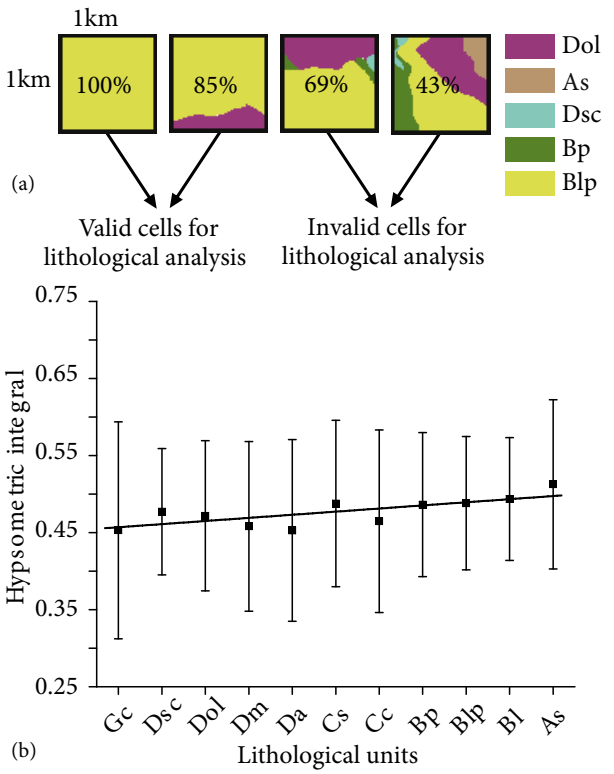

Figure 9. a) Diagram indicating the method for the selection of valid squares for the lithological analysis (proposed by Pérez-Peña et al., 2009b), where only cells where more than 85% of each cell was composed of same rock type are taken into consideration; b) mean hypsometric integral values calculated from 5-m DEM using analysis grid size of 1 km^2 for each lithologic group (described in Table 1). The size of the error bars indicates the standard deviation of the mean HI values for each lithological unit.

unit, the HI mean value shows a minor positive correlation (between high HI values and hard rock type), which agrees with the previous studies of Hurtrez and Lucazeau (1999) and Pérez-Peña et al. (2009b); nevertheless, the standard deviation (or size of error bars) for each HI mean value is too high to consider a positive correlation between these 2 factors. From this analysis, we conclude that, in the study area, the lithological variation is not sufficient to explain large differences in relatively high or low HI values.

5.3. Spatial autocorrelation of the HI values

To analyze spatial autocorrelation patterns between HI values, we calculated Moran's I statistic (Moran, 1950), the expected Moran's I or *E(I)*, and the *Z*-score (Anselin, 1995; Table 2). The results indicate that all the HI values are positively correlated, showing high *Z*-scores, and, therefore, are positioned in clusters in the study area. Moran's I only reveals that the data are positively clustered; this statistic is unable to differentiate that these clusters are of either high values or low values. Therefore, to map the clusters (hot spots and cold spots) of high and low HI values (Figure 10), we applied the Gi*-statistic (Ord and Getis, 1995). A fixed distance of 2.5 km was used to delineate the neighboring cells to correlate adjacent squares that are affected by uplift or subsidence in the hanging and footwall fault blocks (Pérez-Peña et al., 2009b).

5.4. Trend surface analysis

A total of 39,796 sample elevation points from the DEM were used to compute a series of polynomial surfaces (up to the 12th order). These surfaces are treated as simplified terrain elevation models for the study area (Grohmann, 2005; Garrote et al., 2008). The best-fit trend surface is the 11th-order polynomial surface (Table 3). This surface

Table 2. Results of spatial autocorrelation analysis of HI values using Moran's I for the different analysis grids and DEMs.

DEM	Analysis grid	N	I	*E(I)*	Z	P
5 m	500 m	9599	0.066224	–0.000104	38.796127	0.0001
5 m	1 km	2504	0.132466	–0.000399	20.468979	0.0001
30 m	500 m	9599	0.035664	–0.000104	20.919922	0.0001
30 m	1 km	2504	0.093417	–0.000399	14.450765	0.0001
90 m	500 m	9599	0.044596	–0.000104	26.145137	0.0001
90 m	1 km	2504	0.127982	–0.000399	19.776470	0.0001

N is the number of HI values, I is Moran's index for the HI values, *E(I)* is the expected Moran's index for a random distribution, Z is the significance level of Moran's index, and P is the probability that the distribution of data could be randomly generated.

clearly shows a SSW downward trending ramp (Figure 11a). This 11th-order polynomial surface was subtracted from the original DEM (Figure 11b) in order to distinguish areas with anomalously high and low elevations and to observe their spatial correlation with the hypsometric integral and regional geological structures. The SW part of the study area and 2 areas in the northeast part show clear positive anomalies, shown as red and orange patches (Figure 11b). These anomalies are spatially correlated with high HI values (hot spots), showing their association with the regional tectonic structures, and are consistent with an active tectonic control.

6. Discussion and conclusion

Moran's I analysis indicated that the HI values for the Secchia, Panaro, and Reno mountain river basins are clustered, but it was unable to show whether the clusters were of high values or low values. Nevertheless, the Gi*-statistic or hot spot/cold spot analysis of the HI data helped to identify and map zones of high and low HI values (hot spots and cold spots). The hot spots of high HI values (Figure 10) and positive TSA anomalies (Figure 11b) are located in the southwest and northeast of the study area in correspondence to regional faults oriented SE-NW and SW-NE. Hot spots 2, 5, 8, 9, 10, and 11 (Figure 10) are more

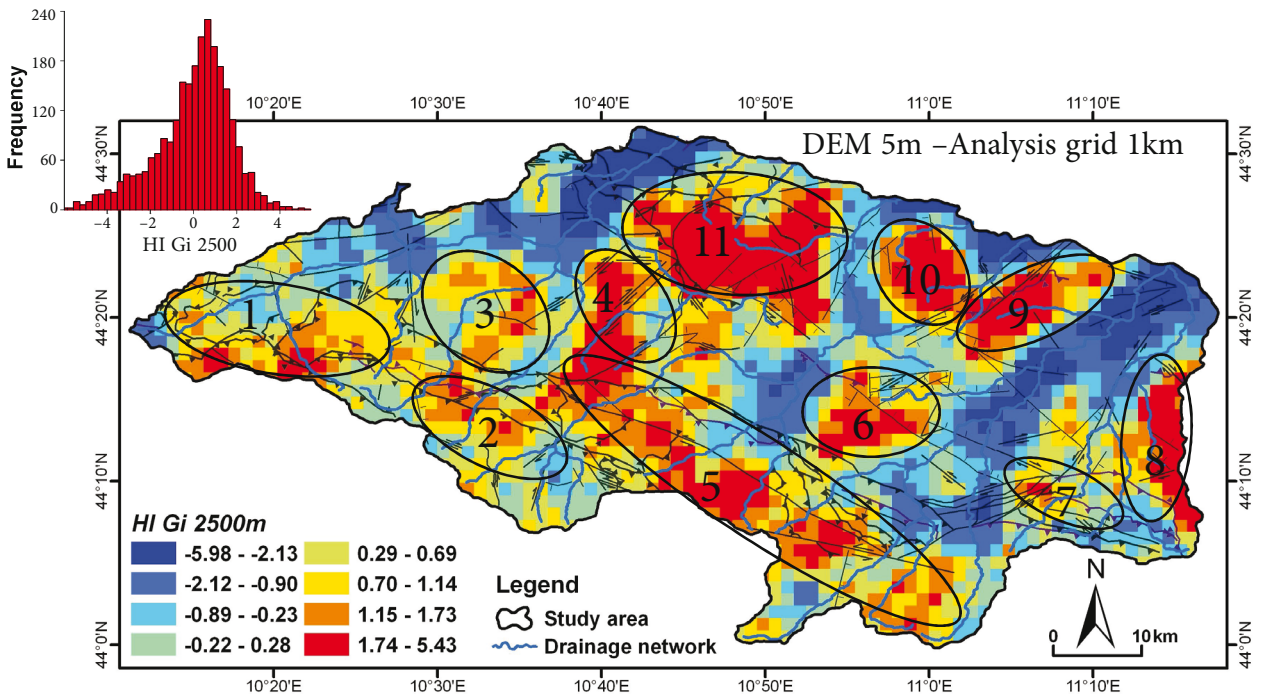

Figure 10. Clusters of high and low HI values identified by Gi*-statistic. The hot spots of high HI values are marked with ovals.

Table 3. RMS values for each trend surface of a given polynomial order for the study area.

Polynomial order	RMS error (m)	Polynomial order	RMS error (m)
1	297.595	7	232.882
2	260.424	8	229.712
3	241.405	9	229.828
4	239.742	10	224.319
5	234.984	11	222.251
6	233.298	12	222.284

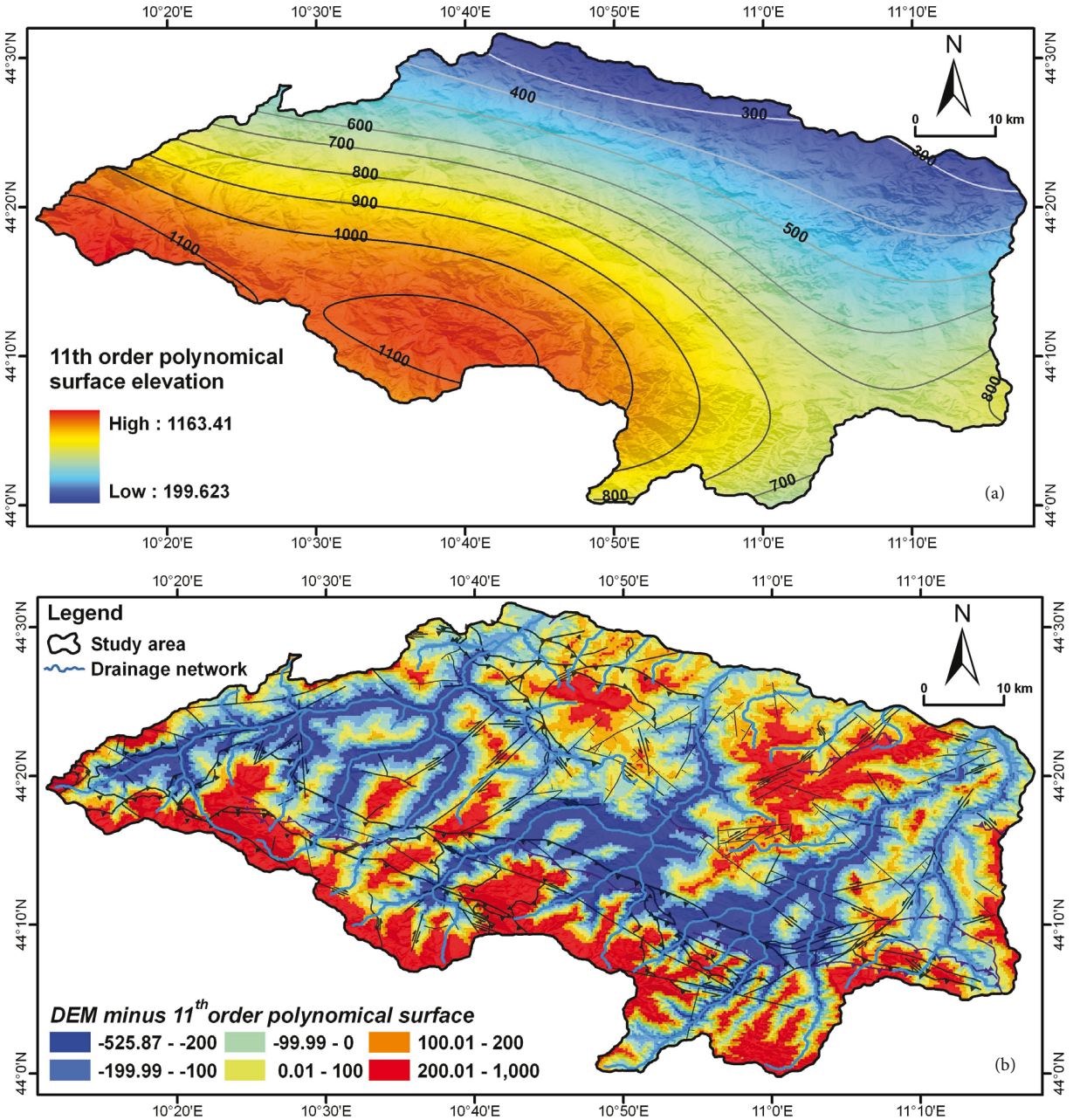

Figure 11. Trend surface analysis maps for the study area: a) 11th-order polynomial surface generated from the 5-m resolution DEM; b) residual map from the subtraction of 11th-order polynomial surface from the DEM.

significant, showing very HI high values concentrated along thrust and strike-slip faults (Michetti et al., 2000; Boccaletti et al., 2004b), where the relative tectonic uplift is also high. These faults are neotectonically active and are associated with numerous historical earthquakes (Bartolini et al., 1982; Ambrosetti et al., 1987; Michetti et al., 2000; Margottini et al., 2007; Figure 12a). The high HI values in the SW part of study area (hot spots 1, 2, 3, and 5; Figure 10) are in correspondence to the out of sequence thrust front that extends from the SE (Castiglion de' Pepoli, Bologna) to NW (Monte Orsaro, Parma), showing morphological evidence of tectonic activity probably as early as the Pliocene (Bendkik et al., 1994; Cerrina Feroni et al., 2002). Hot spot 1 (Figure 10) corresponds to the upper Secchia river basin. Here, the tributaries T. L. Cerretano, T. Ozola, and T. Secchiello have been displaced

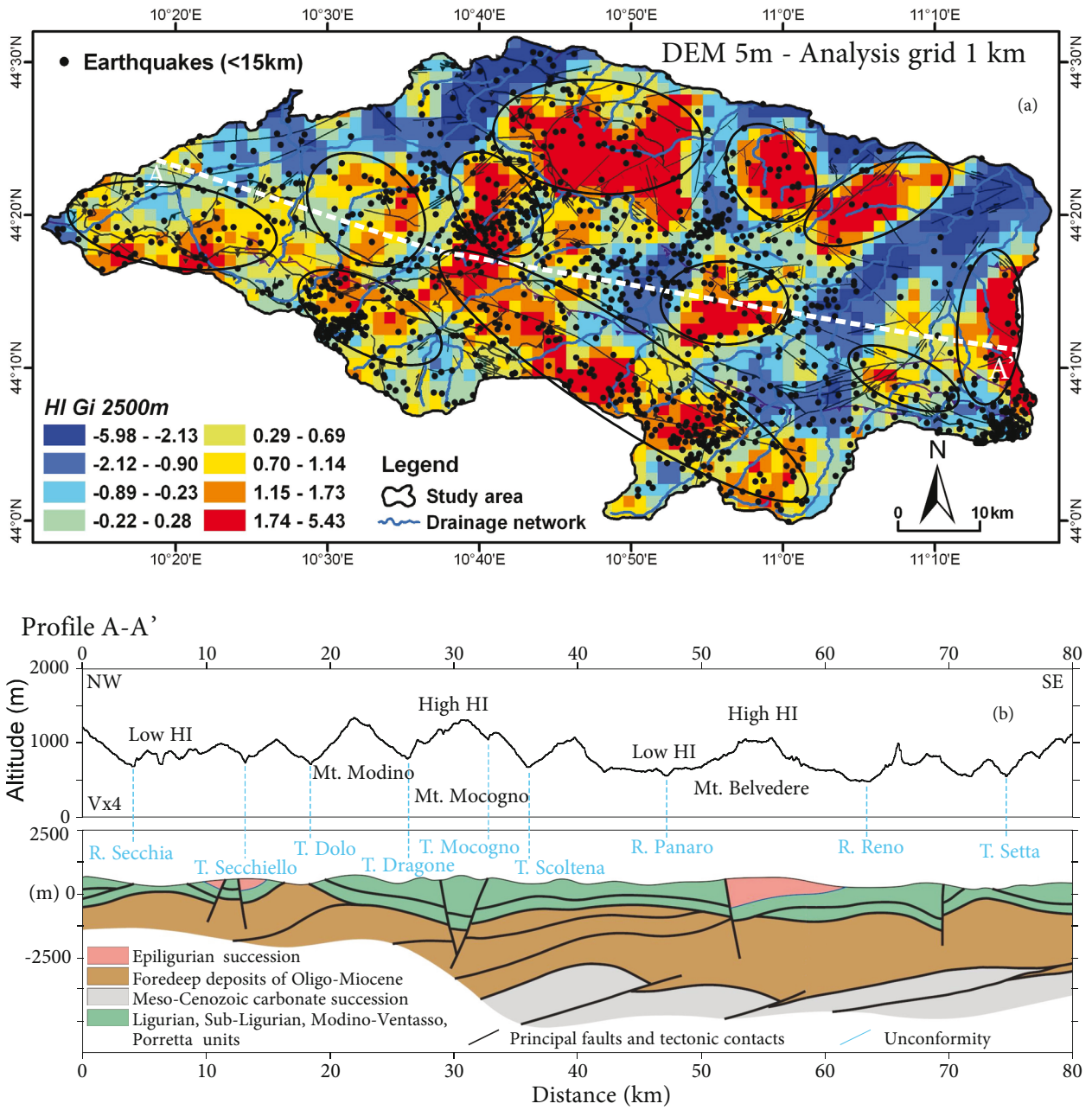

Figure 12. a) Map showing shallow earthquakes (<15 km) for the Secchia, Panaro, and Reno mountain river basins, where the epicenter distribution is much diffused but some clear clusters can be viewed near the active faults; b) SE-NW profile AA′ showing the geological cross-section, various anomalies due to principal faults and tectonic contacts, and the relation between HI values and the topography underneath.

due to the active movements of regional thrust and strike-slip faults (Michetti et al., 2000; Boccaletti et al., 2004b). In this area the stream gradient and steepness are anomalously high, which is associated with relatively high rock uplift rates.

In the middle section of Torrent Dolo (hot spot 3; Figure 10), high HI values and a sudden increase in both steepness and stream gradient are attributed to the activity of deep structures and correspond to the active tectonic window of the Dolo valley (Bettelli et al., 2002a; Boccaletti et al., 2004a). Near Mt. Cimone (hot spot 5; Figure 10), the influence of the structural characteristics on the morphology is also evident, which is in correspondence with the main scarps and ridges (Castaldini et al., 2009). Panizza et al. (1978) assumed that some large landslides in the northern zone of Mt. Cimone could have been controlled by neotectonic discontinuities. The recent tectonic activity of the Mt. Cimone area is also supported by thermochronologic age-elevation relationships for both the apatite fission track and (U-Th)/He thermochronometry (Thomson et al., 2010). Here the rocks of the Macigno Formation are little disturbed by normal faulting. Hot spots 8, 10, and 11 (Figure 10) are also showing clusters of very high HI values; these clusters are correlated to the active strike-slip and normal and thrust faults present in this area (Michetti et al., 2000). Hot spot 11 (Figure 10) is located downstream near the eastern flank of Secchia river valley. This area is marked by a rather continuous NNE-verging and SSW-dipping thrust system (Boccaletti et al., 1985). Historical and instrumental seismicity distribution (Castello et al., 2006) and the dominant reverse earthquake focal solutions (Pondrelli et al., 2006) suggest that frontal thrusts and lateral thrust ramps are potentially seismogenic (Selvaggi et al., 2001; Boccaletti et al., 1985, 2004a; Calderoni et al., 2009). At hot spot 7 (Figure 10), the drainage network is strongly influenced by neotectonic activity. The morphological contrast and signs of fluvial capture around the active anticline of Castiglion de' Pepoli in this area are indicative of the recent tectonic activity, which gives rise to the uplift of this major anticline (Boccaletti et al., 2004a). The high HI and positive TSA anomalies are associated with ongoing tectonic activity and recent uplift of this area (Figure 12b).

HI distribution does not clearly correlate with the diverse range of lithologies, RA, and MA. The clusters of high HI and TSA anomalies are positively correlated with the regional active structures and correspond well with the neotectonic activity of the study area (Boccaletti et al., 2004b). We conclude that the use of LISA for HI analysis and TSAs enable us to mark zones of active deformation that reveal recent tectonic activity in good correspondence to the tectonically uplifted areas.

References

Ambrosetti P, Carboni MG, Conti MA, Esu D, Girotti O, La Monica GB, Landini B, Parisi G (1987). Il Pliocene ed il Pleistocene inferiore del bacino del Fiume Tevere nell'Umbria meridionale. Geogr Fis Dinam Quat 10: 10–33 (in Italian).

Amrhein C, Reynolds H (1997). Using the Getis statistic to explore method aggregation effects in metropolitan Toronto census data. Can Geogr 41: 137–149.

Anselin L (1995). Local indicators of spatial association-LISA. Geogr Anal 27: 93–115.

Balocchi P (2003). Analisi mesostrutturale e macrostrutturale delle strutture fragili presenti nelle unità del gruppo di Bismantova affioranti tra Zocca e Castel d'Aiano (Appennino Modenese e Bolognese). Modena, Italy: Università di Modena e Reggio Emilia (in Italian).

Bartolini C, Bernini M, Carloni GC, Costantini A, Federici PR, Gasperl G, Lazzarotto A, Marchetti G, Mazzanti R, Papani G et al. (1982). Carta Neotettonica dell' Appennino Settentrionale, note illustrative. Boll Soc Geol It 101: 523–549 (in Italian).

Bendkik AM, Boccaletti M, Bonini M, Poccianti C, Sani F (1994). Structural evolution of the outer Apennine chain (Firenzuola-Città di Castello sector and Montefeltro area, Tuscan-Romagnan and Umbro-Marchean Apennine). Mem Soc Geol It 48: 515–522.

Bertolini G, Pellegrini M (2001). The landslides of the Emilia Apennines (northern Italy) with reference to those which resumed activity in the 1994-1999 period and required civil protection interventions. Quad Geol Appl 8: 27–74.

Bettelli G, De Nardo MT (2001). Geological outlines of the Emilia Apennines (Italy) and introduction to the rock units cropping out in the areas of the landslides reactivated in the 1994-1999 period. Quad Geol Appl 8: 1–26.

Bettelli G, Panini F, Capitani M (2002a). Carta Geologico-Strutturale dell'Appennino Emiliano sudorientale. In: The Third Workshop on Geological Mapping, Proceedings, pp. 47–52 (in Italian).

Bettelli G, Panini F, Pizziolo M (2002b). Note illustrative della Carta Geologica d'Italia alla scala 1:50.000, Pavullo nel Frignano, sheet 236. Rome, Italy: Geological Survey of Italy (in Italian).

Blanchard SD, Rogan J, Woodcock DW (2010). Geomorphic change analysis using ASTER and SRTM digital elevation models in Central Massachusetts, USA. GISci Remote Sensing 47: 1–24.

Boccaletti M, Bonini M, Corti G, Gasperini P, Martelli L, Piccardi L, Severi P, Vannucci P (2004a). Note illustrative alla Carta Sismotettonica della regione Emilia-Romagna alla scala 1:250.000. Florence, Italy: CNR (in Italian).

Boccaletti M, Bonini M, Corti G, Gasperini P, Martelli L, Piccardi L, Severi P, Vannucci P (2004b). Carta Sismotettonica della regione Emilia-Romagna alla scala 1:250.000. Florence, Italy: CNR (in Italian).

Boccaletti M, Coli M, Decanadia FA, Giannini E, Lazzarotto A (1981). Evoluzione dell'Appennino settentrionale secondo un nuovo modello strutturale. Mem Soc Geol It 2: 359–373 (in Italian).

Boccaletti M, Coli M, Eva C, Ferrari G, Giglia G, Lazzatotto A, Merlanti F, Nicolich R, Papani G, Postpischl D (1985). Considerations on the seismotectonics of the Northern Apennines. Tectonophysics 117: 7–38.

Boccaletti M, Elter P, Guazzone G (1971). Polarità strutturali delle Alpi e dell'Appennino in rapporto all'inversione di una zona di subduzione nord-tirrenica. Mem Soc Geol It 10: 371–378 (in Italian).

Boccaletti M, Guazzone G (1972). Gli archi appenninici, il Mar Ligure ed il Tirreno nel quadro della tettonica dei bacini marginali retro-arco. Mem Soc Geol It 11: 201–216 (in Italian).

Calderoni G, Di Giovambattista R, Burrato P, Ventura G (2009). A seismic sequence from Northern Apennines (Italy) provides new insight on the role of fluids in the active tectonics of accretionary wedges. Earth Planet Sci Lett 281: 99–109.

Castaldini D, Coratza P, Panizza M (2009). Landslides or moraines? A new geomorphological map of the area of Mt. Cimone (the highest peak of the Northern Apennines, Italy). In: Malet JP, Remaitre A, Bogaard T, editors. Landslide Processes: From Geomorphologic Mapping to Dynamic Modeling. Strasbourg, France: CERG Editions, pp. 9–14.

Castello B, Selvaggi G, Chiarabba C, Amato A (2006). CSI Catalogo della sismicità italiana 1981-2002, version 1.1. Rome, Italy: INGV-CNT (in Italian).

Cerrina Feroni A, Martelli L, Martinelli P, Ottria P (2002). Carta geologico strutturale dell'Appennino Emiliano Romagnolo. Florence, Italy: CNR (in Italian).

Cerrina Feroni A, Martelli L, Martinelli P, Ottria P, Sarti G (2001). The Romagna Apennines, Italy: an eroded duplex. Geol J 36: 39–54.

Chen YC, Sung Q, Cheng KY (2003). Along-strike variations of morphotectonic features in the Western Foothills of Taiwan: tectonic implications based on stream-gradient and hypsometric analysis. Geomorphology 56: 109–137.

Chou YH (1997). Exploring Spatial Analysis in Geographic Information Systems. Santa Fe, NM, USA: Onward Press.

Cliff A, Ord JK (1981). Spatial Processes, Models and Applications. London, UK: Pion Ltd.

Cruden DM, Varnes DJ (1996). Landslide types and processes. In: Turner AK, Schuster RL, editors. Landslides: Investigation and Mitigation. Washington, DC, USA: National Academy Press, pp. 36–75.

Diniz-Filho JAF, Bini LM, Hawkins BA (2003). Spatial autocorrelation and red herrings in geographical ecology. Global Ecol Biogeogr 12: 53–64.

Elter P (1960). I lineamenti tettonici dell'Appennino a NW delle Apuane. Boll Soc Geol It 60: 273–312 (in Italian).

Garrote J, Heydt GG, Cox RT (2008). Multi-stream order analyses in basin asymmetry: a tool to discriminate the influence of neotectonics in fluvial landscape development (Madrid Basin, Central Spain). Geomorphology 102: 130–144.

Getis A, Ord JK (1996). Local spatial statistics: an overview. In: Longley P, Batty M, editors. Spatial Analysis: Modelling in a GIS Environment. Cambridge, UK: GeoInformation International, pp. 261–277.

Grohmann CH (2005). Trend-surfaces analysis of morphometric parameters: A case study in southeastern Brazil. Comp Geosci 31: 1007–1014.

Haining R (1990). Spatial Data Analysis in the Social and Environmental Sciences. Cambridge, UK: Cambridge University Press.

Huang XL, Niemann JO (2006). An evaluation of the geomorphically effective event for fluvial processes over long periods. J Geophys Res Earth Surf 111: 1–17.

Hurtrez JE, Lucazeau F, Lavé J, Avouac JP (1999). Investigation of the relationships between basin morphology, tectonic uplift and denudation from the study of an active fold belt in the Siwalik Hills, central Nepal. J Geophys Res Earth Surf 104: 12779–12796.

Keller EA, Pinter N (2002). Active Tectonics: Earthquakes, Uplift, and Landscape. Upper Saddle River, NJ, USA: Prentice Hall.

Langbein WB (1947). Topographic Characteristics of Drainage Basins. Reston, VA, USA: USGS Water Supply Paper 968.

Lifton NA, Chase CG (1992). Tectonic, climatic and lithologic influences on landscape fractal dimension and hypsometry: implications for landscape evolution in the San Gabriel Mountains, California. Geomorphology 5: 77–114.

Luo W (1998). Hypsometric analysis with a geographic information system. Comp Geosci 24: 815–821.

Luo W (2002). Hypsometric analysis of Margaritifer Sinus and origin of valley networks. J Geophys Res Planets: 107: 50–71.

Margottini C, Spizzichino D, Onorati G (2007). Cambiamenti climatici, dissesto idrogeologico e politiche di adattamento in Italia: un percorso tra passato presente e futuro. Rome, Italy: National Conference on Climate Change (in Italian).

Masek JG, Isacks BL, Gubbels TL, Fielding EJ (1994). Erosion and tectonics at the margins of continental plateaus. J Geophys Res 99: 13941–13956.

Mayer L (1990). Introduction to Quantitative Geomorphology: An Exercise Manual. Englewood Cliffs, NJ, USA: Prentice Hall.

Michetti AM, Serva L, Vittori E (2000). ITHACA (Italy Hazard from Capable Faulting), A Database of Active Capable Faults of the Italian Onshore Territory. Rome, Italy: Internal Report of Agenzia Nazionale Protezione Ambiente.

Moglen GE, Bras RL (1995). The effect of spatial heterogeneities on geomorphic expression in a model of basin evolution. Water Resour Res 31: 2613–2623.

Moran PAP (1950). Notes on continuous stochastic phenomena. Biometrika 37: 17–23.

Ohmori H (1993). Changes in the hypsometric curve through mountain building resulting from concurrent tectonics and denudation. Geomorphology 8: 263–277.

Omvir S (2009). Hypsometry and erosion proneness: a case study in the lesser Himalayan Watersheds. J Soil Water Conserv 8: 53–59.

Ord JK, Getis A (1995). Local spatial autocorrelation statistics: distributional issues and application. Geogr Anal 27: 286–306.

Panini F, Bettelli G, Pizziolo M, Bonazzi U, Capitani M, Fioroni C, Fregni P, Gasperi G, Amorosi A, Fazzini P et al. (2002a). Note illustrative alla Carta Geologica D'Italia alla scala 1:50.000, sheet 237, Sasso Marconi. Regione Emilia-Romagna. Florence, Italy: CNR (in Italian).

Panini F, Bettelli G, Pizziolo M, Bonazzi U, Capitani M, Fioroni C, Fregni P, Gasperi G, Amorosi A, Fazzini P et al. (2002b). Note Illustrative alla Carta Geologica D'Italia alla scala 1:50.000, sheet 237, Sasso Marconi. Regione Emilia-Romagna. Florence, Italy: CNR (in Italian).

Panizza M, Carton A, Castaldini D, Mantovani F, Spina R (1978). Esempi di morfoneotettonica nelle Dolomiti occidentali e nell'Appennino modenese. Geogr Fis Dinam Quat 1: 28–54 (in Italian).

Pérez-Peña JV, Azanon JM, Azor A (2009a). CalHypso: An ArcGIS extension to calculate hypsometric curves and their statistical moments. Applications to drainage basin analysis in SE Spain. Comp Geosci 35: 1214–1223.

Pérez-Peña JV, Azanon JM, Booth-Rea G, Azor A, Delgado J (2009b). Differentiating geology and tectonics using a spatial autocorrelation technique for the hypsometric integrals. J Geophys Res 114: 1–15.

Piccinini D, Chiarabba C, Augliera P (2006). Compression along the northern Apennines? Evidences from the Mw 5.3 Monghidoro earthquake. Terra Nova 18: 89–94.

Picotti V, Pazzaglia FJ (2008). A new active tectonic model for the construction of the Northern Apennines mountain front near Bologna (Italy). J Geophys Res 113: B08412.

Picotti V, Ponza A, Pazzaglia FJ (2009). Topographic expression of active faults in the foothills of the Northern Apennines. Tectonophysics 474: 285–294.

Pike RJ, Wilson SE (1971). Elevation-relief ratio, hypsometric integral, and geomorphic area-altitude analysis. Geol Soc America Bull 82: 1079–1084.

Plesi G, Chicchi S, Daniele G, Bettelli G, Catanzarini R, Cerrina Feroni A, De Nardo MT, Martinelli P, Ottria G, Panini F et al. (2002a). Note illustrative alla Carta Geologica d'Italia alla scala 1:50.000, sheet 235, Pievepelago. Regione Emilia-Romagna. Florence, Italy: CNR (in Italian).

Plesi G, Daniele G, Botti F, Palandri S (2002b). Carta strutturale dell'alto Appennino tosco-emiliano, scale 1:100.000. Florence, Italy: CNR (in Italian).

Pondrelli S, Salimbeni S, Ekstrom G, Morelli A, Gasperini P, Vannucci G (2006). The Italian CMT dataset from 1977 to the present. Phys Earth Planet Int 159: 286–303.

Ratcliffe JH, McCullagh MJ (1998). Identifying repeat victimization with GIS. Br J Criminol 38: 651–662.

Reutter KJ, Groscurth J (1978). The pile of nappes in the Northern Apennines, its unravelment and emplacement. In: Cloos H, Roeder D, Schmidt K, editors. Alps, Apennines, Hellenides. Stuttgart, Germany: E. Schweitzerbart'sche Verlagsbuchhandlung, pp. 239–243.

Rutledge AM, Christensen PR (2010). Hypsometry of lobate debris aprons on the eastern rim of Hellas Basin, Mars: implications for climate variations. American Geophysical Union, Fall Meeting, Abstract No. P51B-1426.

Schumm SA (1956). Evolution of drainage systems and slopes in badlands at Perth Amboy, New Jersey. Geol Soc America Bull 67: 597–646.

Selvaggi G, Ferulano F, Di Bona M, Frepoli A, Azzara R, Basili A, Chiarabba C, Ciaccio MG, Di Luccio F, Lucente FP et al. (2001). The Mw = 5. 4 Reggio Emilia 1996 earthquake: active compressional tectonics in the Po Plain, Italy. Geophys J Int 144: 1–13.

Severi P, Martelli L, Caporale L, Benini A, De Nardo MT, Colalongo ML, Pasini G, Vaiani SC, Bassetti M, Amorosi A et al. (2002a). Note illustrative alla Carta Geologica d'Italia alla scala 1:50.000, sheet 220, Casalecchio di Reno. Regione Emilia-Romagna. Florence, Italy: CNR (in Italian).

Severi P, Martelli L, Caporale L, Benini A, De Nardo MT, Colalongo ML, Pasini G, Vaiani SC, Bassetti M, Amorosi A et al. (2002b). Carta Geologica d'Italia alla scala 1:50.000, sheet 220, Casalecchio di Reno. Regione Emilia-Romagna. Florence, Italy: CNR (in Italian).

Spagnolo M, Pazzaglia FJ (2005). Testing the geological influences on the evolution of river profiles: a case from the northern Apennines (Italy). Geogr Fis Dinam Quat 28: 103–113.

Strahler AN (1952b). Hypsometric (area-altitude) analysis of erosional topography. Geol Soc America Bull 63: 1117–1142.

Thomson SN, Brandon MT, Reiners PW, Zattin M, Isaacson PJ, Balestrieri ML (2010). Thermochronologic evidence of orogen-parallel variability in wedge kinematics during extending convergent orogenesis of the northern Apennines, Italy. Geol Soc America Bull 122: 1160–1179.

Trigila A (editor) (2007). Rapporto sulle frane in Italia. Il Progetto IFFI-Metodologia, risultati e rapporti regionali (reporti 78/2007). Rome, Italay: APAT.

Unwin DJ (1996). GIS, spatial analysis and spatial statistics. Prog Hum Geogr 20: 540–551.

Vai GB, Martini PI (editors) (2001). Anatomy of an Orogen: The Apennines and Adjacent Mediterranean Basins. Dordrecht, the Netherlands: Kluwer Academic.

Van der Beek P, Braun J (1998). Numerical modeling of landscape evolution on geological time-scales: a parameter analysis and comparison with the south-eastern highlands of Australia. Basin Res 10: 49–68.

Walcott RC, Summerfield MA (2008). Scale dependence of hypsometric integrals: an analysis of southeast African basins. Geomorphology 96: 174–186.

Weissel JK, Pratson LF, Malinverno A (1994). The length-scaling properties of topography. J Geophys Res 99: 13997–14012.

Willgoose G, Hancock G (1998). Revisiting the hypsometric curve as an indicator of form and process in transport-limited catchment. Earth Surf Processes Landforms 23: 611–623.

Wilson LJ, Vallee M, Montpetit J (2009). Comments on hydrometeorological accuracy enhancement via postprocessing of numerical weather forecasts in complex terrain. Weather Forecast 24: 892–894.

Wulder M, Boots B (1998). Local spatial autocorrelation characteristics of remotely sensed imagery assessed with the Getis statistic. Int J Remote Sensing 19: 2223–2231.

Yu D, Wu C (2004). Understanding population segregation from Landsat ETM+ imagery: a geographically weighted regression approach. GISci Remote Sensing 41: 187–206.